PNAS Nexus, 2024, 3, pgae252
https://doi.org/10.1093/pnasnexus/pgae252
Advance access publication 30 July 2024
Research Report

Resonance sonomanometry for noninvasive, continuous monitoring of blood pressure

Raymond Jimenez[a,*], Dominic Yurk[b], Steven Dell[a], Austin C. Rutledge[a], Matt K. Fu[a], William P. Dempsey[a], Yaser Abu-Mostafa[b], Aditya Rajagopal[a,b,c] and Alaina Brinley Rajagopal[a,b]

[a]Esperto Medical, Inc., 300 Spectrum Center Drive, Suite 400, Irvine, CA 92618, USA
[b]Department of Electrical Engineering, California Institute of Technology, 1200 East California Blvd, Pasadena, CA 91125, USA
[c]Department of Biomedical Engineering, University of Southern California, 3650 McClintock Ave, Los Angeles, CA 90089, USA
*To whom correspondence should be addressed: Email: raymond.jimenez@esperto.health
Edited By: Tejal Desai

Abstract

Cardiovascular disease is the leading cause of death worldwide. Existing methods for continuous, noninvasive blood pressure (BP) monitoring suffer from poor accuracy, uncomfortable form factors, or a need for frequent calibration, limiting their adoption. We introduce a new framework for continuous BP measurement that is noninvasive and calibration-free called resonance sonomanometry. The method uses ultrasound imaging to measure both the arterial dimensions and artery wall resonances that are induced by acoustic stimulation, which offers a direct measure of BP by a fully determined physical model. The approach and model are validated in vitro using arterial mock-ups and then in multiple arteries in human subjects. This approach offers the promise of robust continuous BP measurements, providing significant benefits for early diagnosis and treatment of cardiovascular disease.

Keywords: ultrasound, continuous noninvasive blood pressure

Significance Statement

Over the last 50 years, various methods have attempted to develop a solution for continuous, noninvasive blood pressure (BP). This manuscript presents a calibration-free, noninvasive, artery-agnostic, and demographic-agnostic method for continuous BP measurement. The method is derived from first principles physics which is complimented by directly observable ultrasound measurements to obtain BP directly and without inference. It also allows for observation of the full, time-varying arterial pressure trace such as would be available from an arterial catheter and has the additional benefit of the capability to measure any artery visible by ultrasound (central and peripheral). This presents a significant advancement in comparison with existing methods requiring compression, catheterization, black-box machine learning, or frequent calibration.

Introduction

Blood pressure (BP) is a critical metric for clinicians when assessing patient health, and as such, continuous, noninvasive measurement has been of long-term interest to the scientific and clinical communities. In an artificial system, fluid pressure would normally be assessed by simply placing a pressure transducer inside the vessel of interest. A similar approach can be applied to human arteries by inserting an arterial catheter, which produces continuous and accurate BP measurements. These continuous waveforms provide significant clinical value which cannot be obtained solely from maximum (systolic) and minimum (diastolic) BP values, including diagnosis of conditions such as aortic stenosis and valve insufficiency (1), measurement of cardiac efficiency (2), and early identification of hypotensive crises (3). However, arterial catheterization is an invasive procedure which is time-consuming and carries risks of pain, infection, hemorrhage, and ischemia (4). As a result, it is typically only performed in critical care units and operating rooms. In all other situations, BP is measured using an inflatable arm cuff, which operates by applying external pressure until the artery collapses (i.e. blood flow stops), and the measurement is taken when pressure is gradually released and blood flow resumes. While these cuffs are noninvasive, they only provide intermittent and often inaccurate measurements compared to measurements from invasive catheters (5–7), and repeated cuff inflation can cause significant discomfort for patients (8). Despite the shortcomings of the BP cuff, it is the

Competing Interest: All authors have varying equity and interest (e.g. current or former employment) in Esperto Medical, the company which sponsored the research and study. Several authors (A.R., A.B.R., D.Y., Y.A.-M., and R.J.) are listed as inventors on patents which cover material in this manuscript.
Received: March 4, 2024. **Accepted:** June 10, 2024

current clinical standard of care worldwide, providing clinicians with critical insight into patients' cardiovascular status.

The limitations of clinical standard BP measurement techniques have inspired the development of numerous continuous, noninvasive BP (cNIBP) measurement techniques based on a variety of physical signals and phenomena (9). These include measurement of fingertip blood perfusion (volume clamping) (10), pressure signals at the surface of the skin (tonometry) (11, 12), light reflectance from blood (photoplethysmography) (13), electrical conductivity of blood (bioimpedance) (14), pressure wave velocity (pulse transit time) (15), reactive forces from cardiac ejection (ballistocardiography) (16), and blood velocity (Doppler ultrasound) (17–21). However, most of these methods require calibration against an inflatable cuff which must be repeated regularly due to dynamic change in BP and arterial physiology (22, 23). Methods that do not require calibration carry drawbacks such as periodic data blackouts (24) or reliance on "black-box" machine learning techniques that may overfit the demographics of the underlying dataset (Table S1 and Supplementary Text S1.1) (25). These constraints significantly limit the ability of these methods to report accurate BP in dynamic conditions such as those found in critically ill patients, where vital signs can rapidly change.

Here, we present a new method for cNIBP measurement based on the phenomenon of resonance sonomanometry (RSM) (Figs. 1, S1). With this method, the artery is stimulated by an acoustic transducer, while its resonant response and dimensions are simultaneously measured using ultrasound imaging (Fig. 1a, b). Our motivation comes from the tuning of a guitar string: change the tension in a string, and its resonant tone changes proportionally to the square root of the tension applied. By plucking the string and measuring the resonant frequency, this relationship can be inverted to calculate the absolute tension applied. We extend this analysis to the circumference of the artery (Fig. 1c). Circumferential wall tension is directly related to fluid pressure inside the artery per Laplace's law, and the specific value of tension can be inferred from the artery's dimensions and resonant frequency. This pressure–resonance relationship is the unique, defining characteristic of the method: applying acoustic stimulus allows determination of the artery's resonant frequency, exposing sufficient information for determination of absolute pressure in an arterial system. This frequency information removes the need for any calibration or external reference.

This model is validated through measurements of an arterial mock-up over a physiologically relevant range of pressures and dimensions. We then show through initial human tests that resonance can be stimulated and can be used to generate BP waveforms on central (carotid) and peripheral (axillary, brachial, and femoral) arteries. These measurements show that the resonance predicted by the physical model not only persists in much more complex in vivo systems, but also that the method produces data with high time resolution, providing continuous, calibration-free measurements of the full absolute (not relative) BP waveform.

Background on the physical model

The physical model draws from two disparate lines of analysis: one from aerospace engineering and the other from biomechanics. The first set of analyses deals with the acoustic resonance modes in thin-walled cylindrical shells for large-scale industrial applications such as fuel tanks and pipelines (26). The second set of analyses examines the dynamics of in vivo arterial walls by modeling them as long, thin-walled cylindrical shells and using structural and fluid mechanics to calculate how these shells respond to changes in pressure (27, 28). While these two lines of analysis share fundamental commonalities and assumptions, no work has combined them to create a model of the resonant modes in pressurized arteries. Furthermore, all of these analyses focus on deriving expected responses based on a known applied pressure. By combining and inverting these relationships, we demonstrate that it is possible to calculate in vivo arterial BP from measurements of a vessel's resonant response.

In order to extend the analysis of inanimate objects (26) to the in vivo context, we used additional mechanical analyses to account for various physical complexities inherent to living systems. These included the presence of a pressurized fluid inside the artery (29) and inertial damping due to fluid mass inside and outside the artery (30, 31). Furthermore, we integrated established biomechanical analyses to account for effects such as the significant distention of the artery as pressure changes and the nonlinear character of its elasticity (27, 28).

Results

Physical model and direct calculation of pressure

Arteries are modeled as an elastic, thin-walled tube; the interior is filled with a fluid (blood) under pressure (with or without flow), and this tube is fixed in a surrounding fluid. We analyze this system and find that the final relation for calculating BP (P) depends on seven parameters: a (artery radius to the center of the wall), h (artery wall thickness), f (artery resonant frequency in Hz), E (arterial wall Young's modulus), ν (arterial wall Poisson's ratio), ρ_S (arterial wall density), and ρ_L (density of fluid surrounding the artery). The first two parameters are commonly measured today using ultrasound imaging, while the last three are nominally consistent across individuals and are estimated from the IT'IS material database for human tissues (32), leaving f and E as the remaining parameters to be determined. f is calculated by fitting our measured frequency response, and E is calculated using the relation $E = (a^2/h)\frac{dP}{da}$, obtained from the Moens–Korteweg and Bramwell–Hill equations (17) (Fig. S2, Table S2, Supplementary Text S1.2). The full pressure equation is given in Equation 1 (see Materials and methods for more on the physical model):

$$P = \frac{9\alpha^4 - 5(3\alpha + \alpha^3)D + 3D^2}{-4(9\alpha - \alpha^3) + 12D} E \tag{1}$$

$$\sim \rho a^2 f^2 \tag{2}$$

where

$$\alpha = h/a \tag{3}$$

$$D = 4\pi^2(1 - \nu^2)\frac{\rho a^2 f^2}{E} \tag{4}$$

$$\rho = \alpha\rho_S + \frac{4}{5}\rho_L \tag{5}$$

In these equations, α and D are the dimensionless thickness and frequency parameters and ρ has units of mass density per unit volume. Equation 1 represents the inverted equation for pressure using the dominant frequency mode, while Equation 2 describes the system's leading-order scaling. These relationships are applicable in the limit when the shell is thin-walled (i.e. $h << a, \alpha << 1$). In particular, the $P \sim f^2$ scaling relation aligns with our intuition

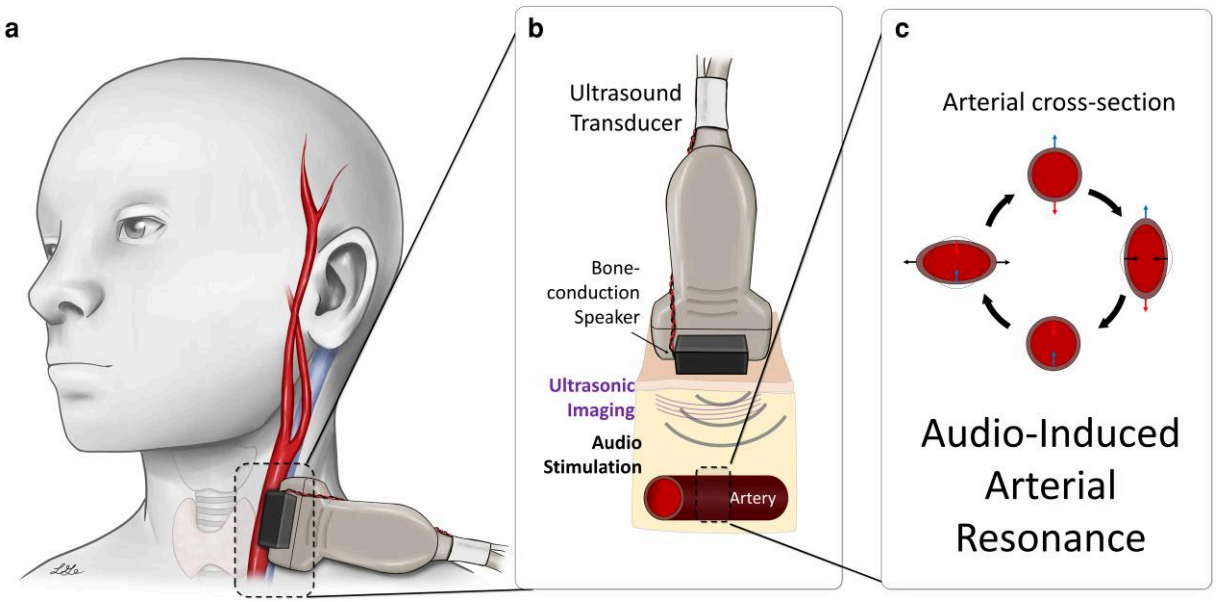

Fig. 1. Acoustic stimulation paired with ultrasound imaging reveals resonance properties of an artery. a) Device placement to measure BP in the carotid artery. b) Illustration of device operation: ultrasound transducer (gray probe) is used to generate images of the artery (at bottom). Width of the transducer array (Acuson 6L3): 44 mm, transducer relative to the artery: 2–3.5 cm depth. The device provides acoustic stimulus via moving-coil drivers (black boxes) which induce arterial response. c) Illustration of RSM. If the frequency of the stimulus aligns with the resonant frequency of the artery, the artery's cross section oscillates between two forms (middle-left and middle-right), exaggerated for clarity. The top and bottom walls of the artery move relative to the ultrasound probe (motion toward and away from the probe are indicated as blue and red, respectively), which is captured by ultrasound imaging. Differential velocity of the walls (top velocity minus bottom velocity) is calculated. Comparing differential wall velocities over a range of stimulus frequencies enables identification of the resonant frequency.

from the guitar string and is further substantiated by the sensitivity analysis (Supplementary Text S1.3); as BP (and therefore wall tension) increases, so too does the resonant tone of the artery.

Validation of physical model in arterial mock-ups

We first validated the pressure–resonance relationship in vitro using a custom device that combined ultrasound imaging and acoustic stimulation (Fig. 1b). We examined resonance in a long, cylindrical arterial mock-up (arterial imaging phantom) fabricated from thin-walled rubber tubing (Figs. 2a, b, S4A). First, we confirmed the presence of the resonance predicted by our model. We inflated the tubing with 75 mmHg of pressure, which is a clinically useful value and swept an acoustic stimulus across a wide range of frequencies while imaging the tubing with ultrasound (Fig. 2c). There were two prominent features in the measured frequency response that are characteristic of resonance: a large spike in magnitude space and a sigmoidal phase response with height π radians, both centered at the same frequency. The presence and sharpness of these features indicated that circumferential resonance was successfully stimulated and measured.

Next, we verified the predicted leading-order behavior of this resonance: an increase in pressure predicts an increase in resonant frequency. The mock-up was inflated to five internal pressures ranging between 95 and 135 mmHg and an acoustic stimulus was swept across a wide range of frequencies while imaging the tubing with ultrasound (Fig. 2d). To determine the frequency of the resonant peak with precision beyond the 10 Hz granularity of our sweep, we applied the Vector Fitting algorithm, which identifies a best fit for the underlying frequency dynamics of a system (33). We then measured the resonant frequency of two mock-ups with different diameters over a range of internal pressures (60–150 mmHg) (Fig. 3). We observed that the resonant frequency increased as internal pressure was increased, in line with predictions from the physical model.

We applied Equation 1 to predict pressure inside the mock-up based on our ultrasound-derived observables. Radius and thickness of the mock-up were measured at each pressure by analyzing the ultrasound imagery. The elastic modulus of the mock-up's wall was computed by observing change in the pressure estimate versus the change in radius (see text describing the Gauss–Seidel method for E estimation in Materials and methods and on the robustness of our estimation procedure in Supplementary Text S1.2 for more detail); this result was found to be in good agreement with independent tensometer measurements. Figure 3a contains several pressure–frequency curves (different curve colors), demonstrating that the model correctly captures the effects of resonant frequency at different arterial dimensions. Figure 3b depicts pressure as calculated by Equation 1 versus the gauge pressure; the inset plot shows the error between the two. Across all measurements, the mean error between the values calculated via the physics model and the measured gauge pressure was −1.09 mmHg with a SD of 1.98 mmHg.

Validation of physical model in humans

While mock-ups allowed us to validate our model in a controlled setting, human arteries and physiology are considerably more complex. BP in the human body is far from constant, rapidly fluctuating from its peak at systole [systolic blood pressure (SBP)] to the diastolic minimum [diastolic blood pressure (DBP)] over a single heartbeat. Additionally, artery walls are not simple elastic membranes free-floating in a homogenous medium; they are made up of multiple anisotropic layers and embedded in other tissues. To determine whether arterial resonance persists in vivo, we applied this methodology on the carotid artery in the neck. As the BP cuff is the current clinical standard of care, we use the

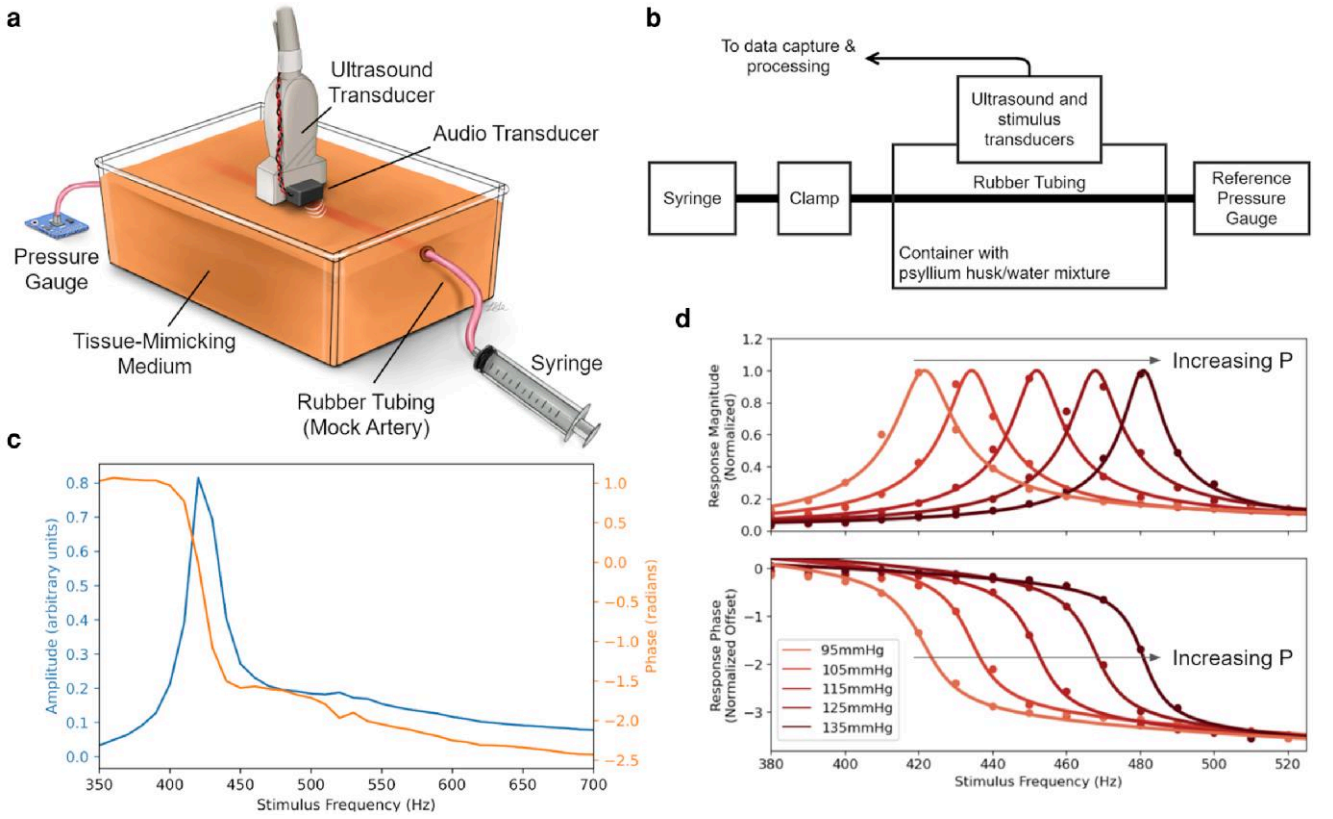

Fig. 2. Resonance response in artery mock-up. a) Illustration of mock artery, showing relative positioning of components. Tubing is 2.18 mm in diameter, with a wall thickness of 0.25 mm, and is placed 2–3 cm below the transducer head. b) System diagram, displaying connection between components. Thin latex rubber tubing filled with water connects a syringe and a digital pressure transducer. The syringe is depressed, increasing the pressure, and clamped once the desired pressure is reached. The rubber tubing is placed in a bath of psyllium husk/water mixture, which serves as a scattering medium to simulate surrounding tissue. c) Magnitude (blue) and phase (orange) response of an arterial mock-up inflated to 75 mmHg. Phase is measured relative to stimulus. d) Extending the measurements of magnitude (top) and phase (bottom) response across multiple mock-up pressures. Raw data points are plotted (circles) as well as their best-fit function provided by the Vector Fitting algorithm (33) (solid lines). Use of a fitting algorithm allows precise determination of peak location below the granularity of the frequency sweep (10 Hz steps).

intermittent measurements from this device to give context to the BP results we generate from each experiment in this section.

A representative frequency response from a human carotid artery using acoustic stimulation is shown in Fig. 4a–d) (image of experimental setup in Fig. S4B). Not only did the expected resonant behavior exist in vivo, but we were also able to resolve variations in this behavior over the course of the cardiac cycle. Arterial dimensions were estimated from feature detection and tracking in the B-mode imagery (Fig. S3). To reduce noise, raw radius and wall velocity estimates were combined using a linear Kalman filter to produce more consistent radius measurements. Raw pressure values were calculated at a rate of 200 Hz and then smoothed with a 20-Hz low-pass filter to produce final outputs. Acoustic stimulus was provided by a repeating, multifrequency waveform with a 50-ms period (equivalent to 20 Hz).

We successfully applied the method to the carotid artery (Fig. 5a, Movie S1) as well as several peripheral sites: the axillary (Fig. 5c), brachial (Fig. 5e), and femoral (Fig. 5g). RSM was stimulated and observed across all four artery sites; the resonant frequencies in Fig. 5b, d, f, and h (for the carotid, axillary, brachial, and femoral, respectively) vary throughout the cardiac cycle synchronously with the corresponding arterial radius measurements. At all four sites, RSM produced BP measurements in a single subject that were broadly in line with those obtained from an oscillometric cuff. Consistent with the physical model, the narrower cross section of the brachial artery induces higher resonance frequencies (450–550 Hz) compared to those in the larger femoral and carotid arteries (~270–350 Hz). For all measurements, the fitted resonant frequency was found to increase with the BP during systole and then decrease again with diastole, synchronous to pulsation in arterial radius (Fig. 5b, d, f, and h) and consistent with the model.

Additional preliminary testing was conducted on the carotid arteries of six human subjects, revealing similar frequency responses to the audio stimulus. We find that RSM captures complete BP waveforms in all six subjects, across genders and a small set of ages (Table S3). Figure 6 shows continuous BP waveforms in 5-second windows from all six subjects. When examining longer interval time windows (Fig. 6g), slower oscillations are sometimes present in the trace, which could be consistent with respiratory oscillations, errors in measurement due to slow drifting motion with the handheld device, or even accuracy limitations of the RSM method itself. Critically, unlike the BP cuff, the RSM method is not constrained to just measurements of systolic or diastolic pressure. In Fig. 6, we also show the close agreement between our direct, *calibration-free* cNIBP measurements using RSM (blue curves) alongside a previously published *calibration-dependent*, inference-based approach to continuous BP from a cuff (black lines) (34).

Because the device was designed specifically for larger vessels (e.g. carotid), device contrast was not sufficient for consistent imaging of smaller vessels (e.g. brachial, radial). The comparison of carotid artery BP to a brachial BP cuff does not allow for comparison of SBP directly due to pulse amplification in peripheral vessels

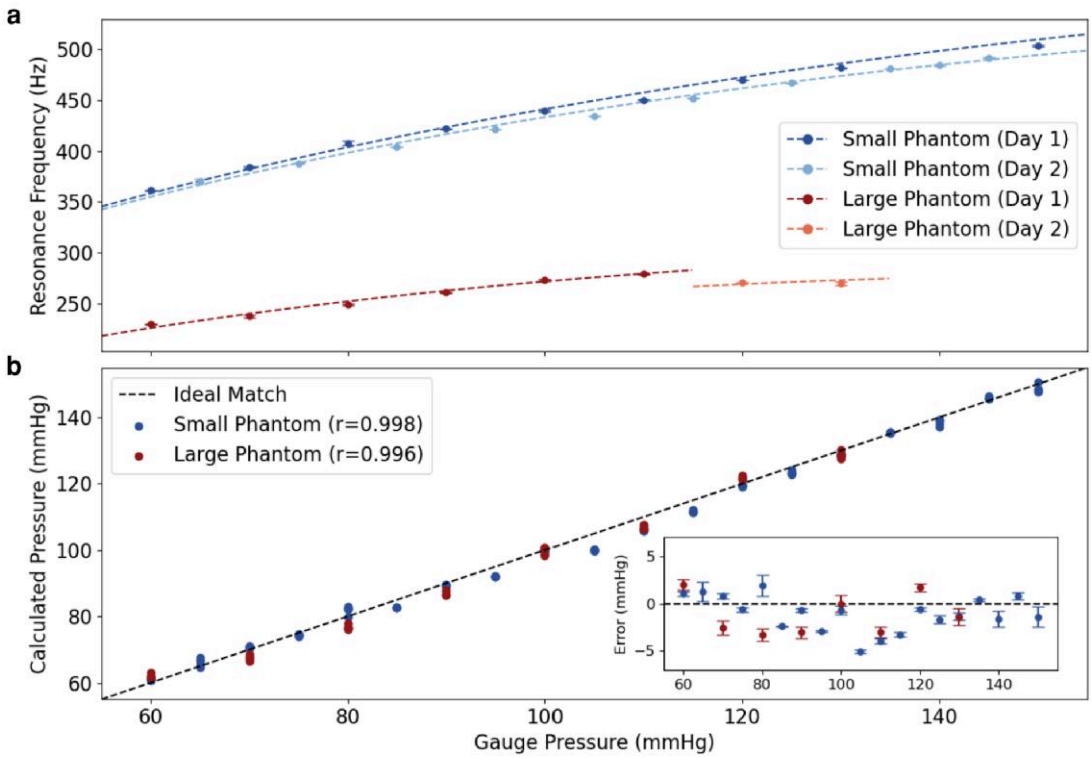

Fig. 3. Comparison of predictions from the physical model and in vitro measurements. a) Resonant frequency as a function of pressure, measured across two mock-ups with different radii. Blue and red markers indicate experimental data for small and large tubing, respectively. Dashed lines indicate predictions from the physical model. Data are separated by day as the mock-up was stored pressurized overnight, resulting in the next day's experiments having a different zero-pressure diameter over the two different experiments. b) Correlation between prediction from the physical model using RSM and imaging data versus the measured (gauge) pressure in the mock-up. Bottom right inset shows the deviations of the model pressure from the measured pressure in the mock-up. Markers and error bars denote mean and SD of repeated trials ($N = 5$ per data point).

(35, 36). Consequently, the primary metric for comparison in this study is the DBP. The SBP values were significantly different ($P < 0.001$), as expected for measurement on a central versus peripheral arterial site; however, the DBP was not significantly different ($P = 0.54$) (Fig. 7).

Discussion

In this study, we have demonstrated that RSM is a physical phenomenon predicted by classical mechanics and can be applied to the continuous measurement of BP in human arteries. Previous studies have demonstrated that ultrasound-based techniques can determine relative changes in BP, but passive ultrasound imaging alone is insufficient to establish an absolute baseline for pressure (17–21, 34). By perturbing the system with an acoustic stimulus, the method can obtain absolute BP without calibration to a reference device. Aside from measurements of SBP and DBP, the method is also able to obtain BP on a 50-ms basis, capturing the shape of the full BP waveform. This waveform can yield significant information that is not available from cuff measurements (1–3, 37).

We first validated the physical model in vitro using simple mock arteries where the material properties and dimensions could be controlled and verified. The model predicted pressures in agreement with the control pressure over a biologically relevant pressure range. Furthermore, we found that the model compensated for creep caused by stress relaxation in both mock arteries, indicating that the model correctly accounts for changes in arterial radius versus resonant frequency.

We then stimulated and detected RSM in vivo in four different arteries of a human subject and produced BP measurements consistent with those from a BP cuff. These results suggest that measuring continuous BP using this approach extends to other arteries and is not necessarily limited by size or location. A good qualitative agreement was observed between the device measurements (e.g. brachial) and those obtained from the BP cuff (Fig. 5). Measurements obtained at the carotid artery return lower systolic values than the BP cuff, which is consistent with the carotid artery being located more centrally than the brachial artery but may also reflect error in BP estimation from the RSM method. Second, our method may be capable of detecting the modest low-frequency variations (~0.1 Hz) in BP associated with the subject's respiration (low-frequency variability in Fig. 6g is consistent with respiration), but further evidence will be needed in future before being certain that these oscillations are due to intrathoracic pressure differences and not just due to a lack of precision in the RSM method itself.

We focused on the carotid artery for the majority of our in vivo tests, as the carotid is a comparatively large and superficial vessel, making ultrasound measurements simpler to obtain, allowing us to evaluate the validity of the physical model more readily. Additionally, noninvasive measurements of central arterial pressure have significant scientific and clinical interest (2, 38–42) and are simply not possible with other popular methods such as volume clamping or photoplethysmography. Since the carotid is more central than arteries targeted by oscillometric cuffs (brachial artery in the upper arm) or arterial catheters [most often the radial artery in the wrist or femoral artery near the groin

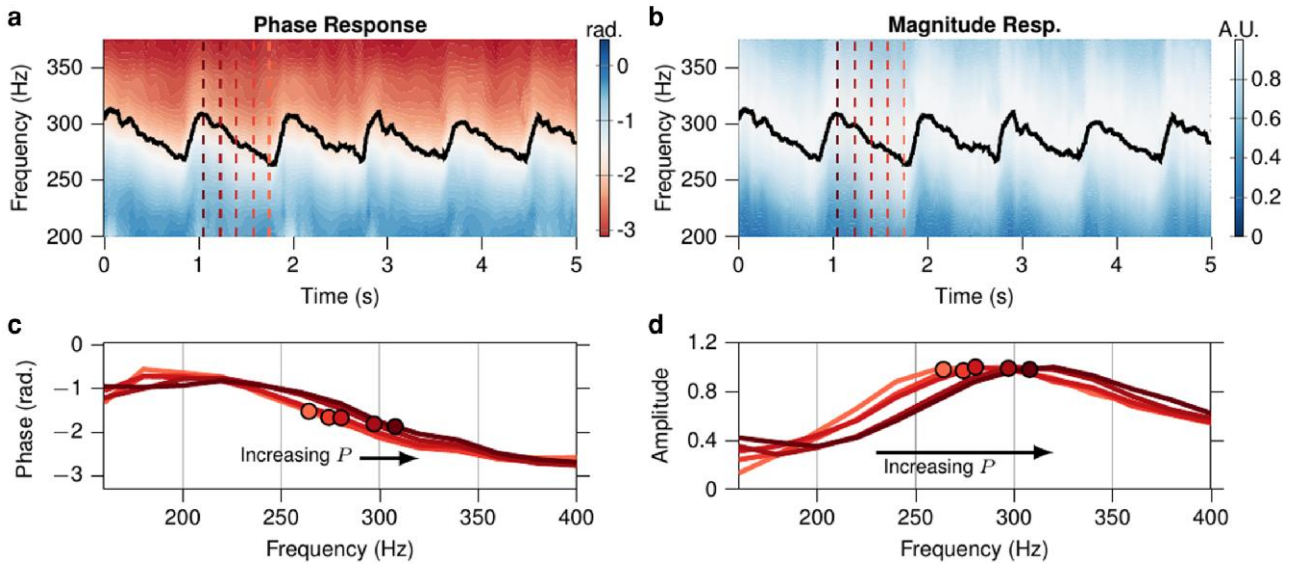

Fig. 4. Excerpts of in vivo RSM from external audio-frequency stimulation data. a) and b) show contour maps of the phase and magnitude response, respectively, as a function of frequency over a 5-second window in a single subject. Solid black lines in these panels indicate the fitted resonant frequency. c) and d) are magnitude and phase response plots corresponding to time instances marked with the dashed red lines in panels a) and b), with darker shades of red corresponding to higher pressure.

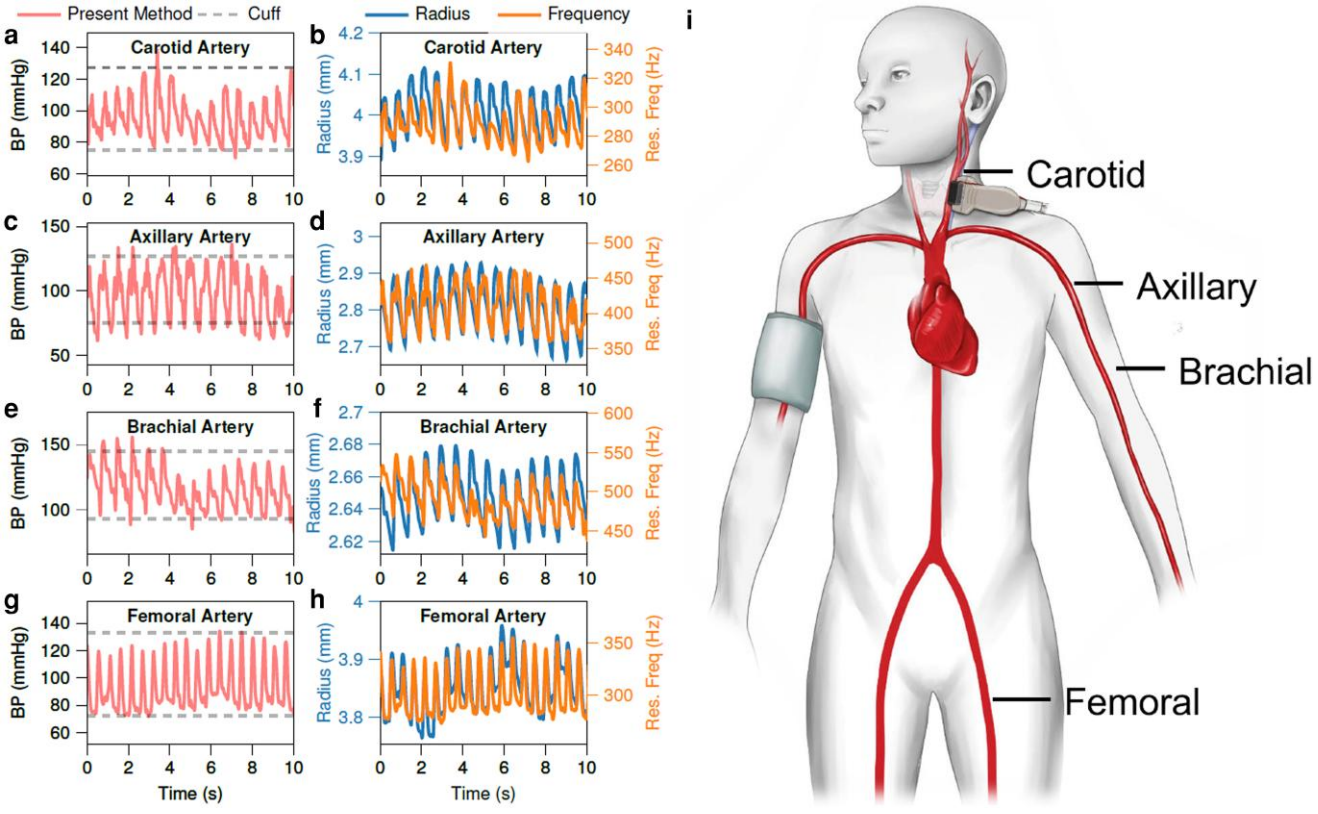

Fig. 5. Comparison of predictions from the physical model and in vivo measurements. Measurement in carotid, femoral, and brachial arteries in one subject. a), c), e), g) BP waveforms (red) taken from four artery locations (carotid, axillary, brachial, and femoral, respectively) in a single subject compared with SBP and DBP obtained from an oscillometric cuff on the brachial artery (gray dashed lines). b), d), f), h) Control pressures from the BP cuff were: carotid (127/75), axillary (127/75), brachial (145/93), and femoral (133/72). Measurements of arterial radius (blue) and resonant frequency (orange) corresponding to the BP waveforms in panels a), c), e), and g). i) Diagram indicating the relative location of each artery. Note that because the BP cuff can only measure SBP and DBP intermittently, the values are extrapolated as constant values.

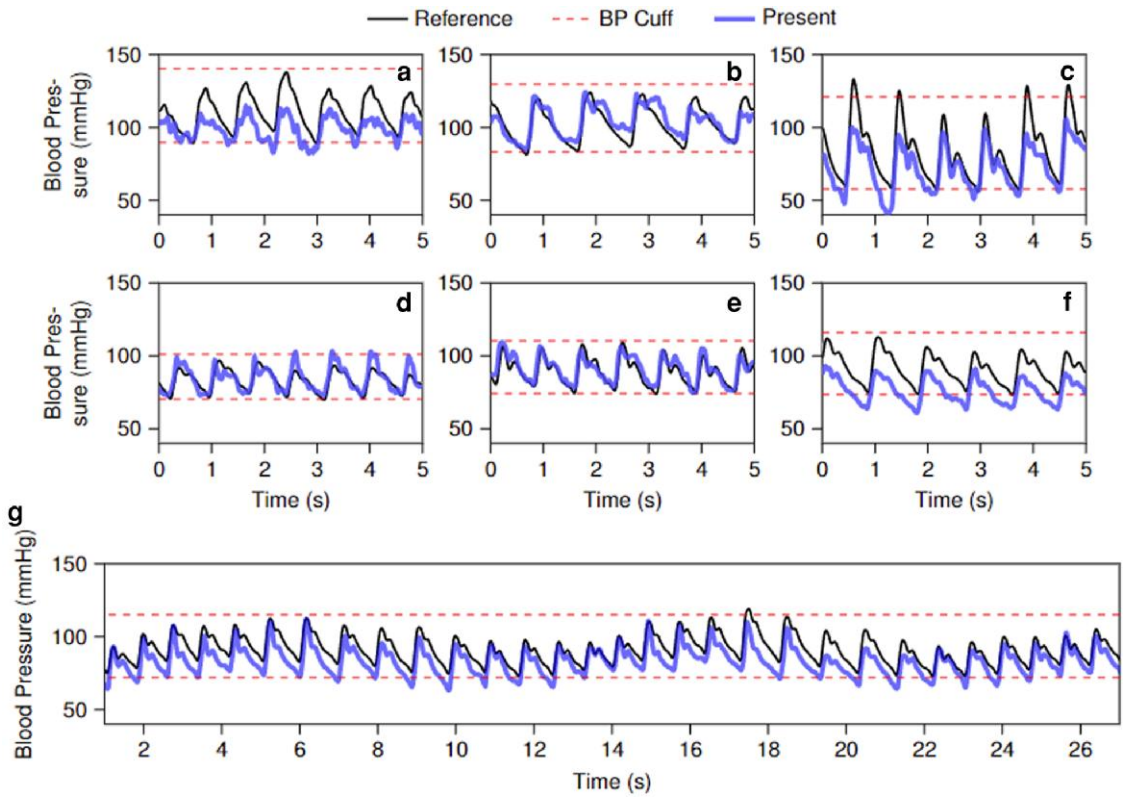

Fig. 6. Representative waveforms of carotid pressure. Excerpts of in vivo data from the six subjects low-pass filtered at 25 Hz. Panels a)–f) correspond to excerpts from Subjects A–F, respectively. Each panel shows 5 seconds of pressure waveforms calculated by the present method, shown in blue, along with the reference systolic and diastolic pressures from the BP cuff, shown in red dashed lines. Panel g) shows a full 30-second time course of BP measurements, and the slow oscillatory behavior underlying the trace is consistent with the variation in BP seen when a subject (Subject F) breathes in and out (~2 breaths in the 30-second window). For comparison, the extrapolated pressure waveform pressure predicted by (34) is shown in solid black. Note that because the BP cuff can only measure SBP and DBP intermittently, the values are extrapolated as constant values.

a

	Mean of Differences	p-value	Mean Value [SD]
DBP VRR (Carotid)	-2.1	0.54	69.6 [8.4]
SBP VRR (Carotid)	-22.7	$<$0.001	97.4 [12.9]

All values except p-values are given in units of mmHg

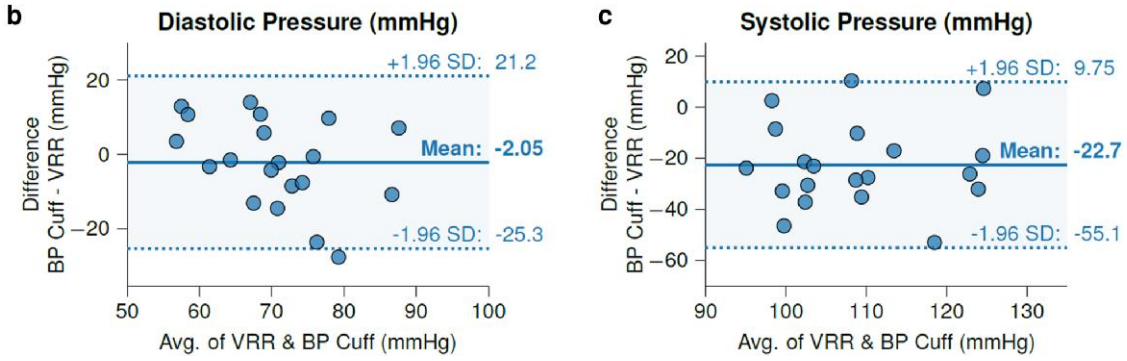

Fig. 7. In vivo measurement results for carotid RSM versus brachial cuff in six subjects. a) displays combined statistical values for RSM versus BP cuff. Bland–Altman plots of DBP (b) and SBP (c) for the carotid RSM to brachial cuff comparison.

(43)], simple and noninvasive pressure measurements in the carotid could provide more insight for clinicians into the progression of cardiovascular disease.

A sensitivity analysis (Supplementary Text S1.3) was conducted in order to assess for potential sources of error, which identified frequency and radius as leading-order terms with a scaling comparable to Equation 2. Although the stimulus is in the audio-frequency range, transmission is coupled to the skin; thus, external audio stimuli (e.g. from ambient conversation) have no effect on extracting resonant frequency (Supplementary Text S1.4). Further, the Vector

Fitting approach has been previously shown to be robust for identifying resonant frequency (33). In contrast, radius is likely a significant source of error in the present implementation due to the positioning (along the length of the artery instead of across) of the manually operated prototype device. However, minor disagreements with the cuff such as is seen in Fig. 6f (blue curve versus dashed lines) may actually indicate physiological changes in this individual's cNIBP trace as a consequence of e.g. relaxation or respiration, demonstrating the power of the approach to show subtle variation in SBP and DBP in time not achievable by the cuff alone. Unlike the RSM approach, the reference method-based result plotted in the same figure (black curve) is forced into a potentially biased BP range enforced by the cuff as a standard (44, 45). However, we cannot completely rule out that the differences observed between the prototype RSM device and the cuff may be due to limitations in the physical model. Future device implementations targeting more peripheral arteries (e.g. radial) will allow us to directly assess and validate similar BP fluctuations, ideally using the continuous gold-standard arterial catheter as a reference.

A major strength of the RSM method lies in the small number of observables required: arterial radius, thickness, and resonant frequency. The BP output is determined by utilizing these observables in real-time, without cuff information, prior training data, or any input of demographic information (e.g. body mass index (BMI), age, gender, etc.). The findings also demonstrate that unlike other methods, RSM is not limited to a single peripheral artery but can be used in both central and peripheral arteries and is likely available to any artery visible by ultrasound. As mentioned, the current early prototype device was optimized for the carotid artery, but even this device was capable of demonstrating the RSM method in vivo in three comparatively smaller, more peripheral arteries (axillary, brachial, and femoral in $N = 1$ subject, Fig. 5). Future adjustments to the prototype design such as increasing the ultrasound frequency and optimizing transducer element design will enable targeting of even smaller arteries (e.g. the radial artery in the wrist). Because the application of this approach is straightforward and based on directly observable characteristics, efforts in the future will focus on developing wearable, easy-to-operate devices (on the arm and/or wrist) that leverage the RSM method, enabling future adoption of the method for a variety of hospital applications (e.g. BP monitoring of critically ill patients, remote patient monitoring, etc.).

Materials and methods

Physics model

To determine the resonance versus pressure relationship, we model our system as a long, thin-walled cylindrical shell (i.e. $L >> a$ and $a >> h$). We assume that this shell has a uniform radius and thickness along its length and that it is surrounded by incompressible fluid. Such a system will support many natural modes of wall motion, each composed of a superposition of an axial component consisting of $m/2$ wavelengths along the length of the cylinder and a circumferential component consisting of n wavelengths around the circumference of the cylinder, where m is an integer equal to or greater than 1 and n is an integer greater than 1. In cylindrical coordinates of axial location z and azimuthal angle θ, the radial displacement w of each point on the surface at any given time t can be expressed as a superposition of sinusoidal basis functions given by

$$w(z, \theta, t) = \Sigma_{m,n} A_{mn} \sin\frac{m\pi z}{L} \cos n\theta \cos 2\pi f t \tag{6}$$

for some scalar amplitude A_{mn}. The general solutions for the equations of motion of this system are quite complex for arbitrary m and n. In a system with $L >> a$, however, the contributions of the axial modes are greatly suppressed compared to the circumferential ones. Neglecting terms proportional to a/L, the resonant frequencies take the form of roots of a cubic polynomial (29):

$$0 = \kappa^3 - K_2\kappa^2 + K_1\kappa - K_0 \tag{7}$$

$$\kappa = \frac{4\pi^2\rho_S a^2(1-\nu^2)}{E} f^2 \tag{8}$$

$$K_0 = \frac{h^2(1-\nu)}{24a^2}(n^8 - 2n^6 + n^4) + \frac{Pa}{Eh}\alpha_1 \tag{9}$$

$$K_1 = \frac{1-\nu}{2}(n^4 + n^2) + \frac{h^2}{12a^2}\alpha_2 + \frac{Pa}{Eh}\alpha_3 \tag{10}$$

$$K_2 = 1 + \frac{3-\nu}{2}n^2 + \frac{h^2}{12a^2}(n^4 + n^2) + \frac{n^2}{1-\nu^2}\frac{Pa}{Eh} \tag{11}$$

$$\alpha_1 = \frac{1-\nu}{2}\left[\left(1 - \frac{h^2}{12a^2}\right)n^6 - n^4\right] \tag{12}$$

$$\alpha_2 = \frac{3-\nu}{2}n^6 - \frac{3+\nu}{2}n^4 + n^2 \tag{13}$$

$$\alpha_3 = \left(\frac{3-\nu}{2} - \frac{h^2}{12a^2}\right)n^4 - n^2 \tag{14}$$

where κ, K_i, and α_i are the dimensionless parameters.

In a damped system, the lowest frequency resonant mode is generally the easiest to excite as first-order damping forces will increase with frequency for a given magnitude of displacement; thus, we focus our attention on the $n = 2$ mode. Finding the smallest real root of Equation 7 and converting from κ back to f with $n = 2$ yield

$$f_{vac}^2 = \frac{C_0 - \sqrt{C_0^2 - C_1}}{24\pi^2(1-\nu^2)ha^4\rho_S} \tag{15}$$

$$C_0 = 5Eh(3a^2 + h^2) + 12a^3P \tag{16}$$

$$C_1 = 12Ea^2h(36a^3P - 4ah^2P + 9Eh^3) \tag{17}$$

The frequency here is labeled f_{vac} because it represents the natural frequency of the cylinder in a vacuum. However, in our system the shell both contains and is surrounded by fluid with nonzero mass, which adds to the effective inertia of the wall as it resonates. For a system with $L >> a$ and $c >> f_{vac}a$, this adds a simple proportional correction to find the natural frequency of the system with fluid (31):

$$\frac{f^2}{f_{vac}^2} = \left[1 + \frac{2n}{n^2+1}\frac{\rho_L}{\rho_S}\frac{a}{h}\right]^{-1} \tag{18}$$

$$f^2 = \frac{C_0 - \sqrt{C_0^2 - C_1}}{24\pi^2(1-\nu^2)a^3\delta} \tag{19}$$

$$\delta = ah\rho_S + \frac{4}{5}a^2\rho_L \tag{20}$$

Inverting Equation 19 to solve for P yields

$$P = \frac{9\alpha^4 - 5(3\alpha + \alpha^3)D + 3D^2}{-4(9\alpha - \alpha^3) + 12D} E \tag{21}$$

$$\alpha = h/a \tag{22}$$

$$D = 4\pi^2(1 - \nu^2)\frac{\rho a^2 f^2}{E} \tag{23}$$

$$\rho = \alpha\rho_S + \frac{4}{5}\rho_L \tag{24}$$

To gain some intuition about the behavior of this pressure equation, we can linearize it for small D, yielding

$$P \sim \rho a^2 f^2 - O(\alpha^3 E) \tag{25}$$

Typical BPs range from 5 to 40 kPa (40–300 mmHg) (46), and typical carotid Young's moduli range from 100 to 1,000 kPA with lower stiffness values at diastole (47). Thus, our calculation of pressure is dominated by the measurement of resonant frequency and radius in the regime of $\alpha \lesssim 0.1$.

Measurement technique

Calculating BP using Equation 21 requires knowledge of seven system parameters: radius, wall thickness, resonant frequency, wall Young's modulus, wall Poisson's ratio, wall density, and fluid density. The first two parameters are routinely measured today using ultrasound imaging (48). In practice, thicknesses were calculated as $h = \bar{h} \times \bar{a}/a$ (where overlines represent temporal averages), relying on the incompressibility of the arterial wall. Parameters 5–7 can be assumed to hold nearly constant (32, 49, 50). This leaves two parameters, resonant frequency and Young's modulus, which must be calculated by more involved means. Young's modulus is discussed in more detail below; the robustness of our estimate in discussed further in Supplementary Text S1.2. See Supplementary Text S1.3 for further analysis of the sensitivity of the BP estimate to the various parameters and constants for measurements conducted in the carotid artery.

Resonant frequency

Previous work has found that high-speed ultrasound imaging is capable of measuring the propagation of shear waves down the length of the arterial wall (51). We instead apply high-speed Doppler ultrasound imaging to measure the strength of wall motion around the arterial circumference under stimulation at various frequencies. While stimulus is applied via audio-frequency transducers, we simultaneously measure the velocities of the top and bottom arterial walls using a separate ultrasound transducer and standard Doppler velocimetry techniques (52). A lock-in amplifier (for static in vitro data) or Fourier transform (for time-varying in vivo data) is used on v_{diff} to extract magnitude and phase of the motion response at the stimulus frequency. The set of magnitude and phase values at all stimulus frequencies represents the frequency response of our system.

In order to extract a resonant frequency from this frequency response, we apply a method from electrical systems analysis known as Vector Fitting. In general, the frequency response $H(f)$ of any system can be approximated as a sum of rational functions:

$$H(f) = \Sigma_{m=1}^{N} \frac{r_m}{if - a_m} + d + fe \tag{26}$$

where f is the frequency, a_m and r_m are the complex poles and residues respectively, and d and e are the real linear offset parameters. In particular, a resonant system will have a complex conjugate pair of poles. Vector Fitting is an algorithm which uses iterative least-squares fitting to find an optimal set of values for (r_m, a_m, d, e) which best match the observed frequency response of the system (33). The final fitted resonant frequency of the system is represented by the magnitude of our complex conjugate pair of poles. If resonance is not present, the Vector Fitting algorithm will return a set of purely real poles; this is additional confirmation that our data contain resonant behavior.

Young's modulus

Previous studies focused on calculating arterial Young's modulus in vivo have utilized the Moens–Kortweg (first term) and Bramwell–Hill (last term) equations, which are related but independent measures of pulse wave velocity down the length of the artery (17):

$$c = \sqrt{\frac{Eh}{\rho_L d}} = \sqrt{\frac{A}{\rho_L}\frac{dP}{dA}} \tag{27}$$

where c is the pulse wave velocity, d is the arterial diameter, and A is the arterial cross-sectional area. Rearranging the latter two terms and substituting $A = \pi a^2$ yield a useful equation for calculating Young's modulus based on changes in pressure:

$$\frac{Eh}{2a} = \pi a^2 \frac{dP}{2\pi a da} \tag{28}$$

$$E = \frac{a^2}{h}\frac{dP}{da} \tag{29}$$

Prior studies calculated dP/da using ultrasound imaging to measure a and an external reference device such as a cuff or tonometer to measure P. We replace this external reference with pressure measurements generated by our device. This creates a recursive relationship, as these pressure measurements are themselves dependent on the value of E we measure. This interdependency can be resolved using the Gauss–Seidel method. First, a physiologically reasonable value for E is chosen as a starting point, and P is calculated at all radii based on this value using Equation 21. These P values are then used to calculate E using Equation 28. By repeating these two steps, both P and E converge on a self-consistent set of values which satisfy both Equations 21 and 28 (e.g. Fig. S2, Table S2).

An important facet of this method of measuring E is that it does not require E to be constant across different radii. Instead, it provides instantaneous E estimates at the same rate that pressure measurements are generated. Real arteries have been found to exhibit substantial variation in E between systole and diastole (47), making dynamic E measurement essential to obtaining accurate pulse pressures. Note that the ultrasound-based approach for radius measurement with RSM gives sufficient resolution to calculate dP/da for each timepoint in the continuous trace for individuals with pulsatile blood flow (e.g. Fig. S3G–L; Movie S1).

Artery mock-up setup

To validate the RSM method physics model, we used compliant, thin-walled rubber tubing, sourced from latex rubber balloons (Qualatex 160Q or similar) to simulate human vasculature. Tube-in-gelatin mock-ups are often used as an ultrasound teaching aid as they provide similar imaging properties to blood vessels embedded in tissue (53, 54). We substituted a water/psyllium fiber

(Metamucil) mixture (55) for the gelatin/psyllium fiber mixture, as tubing can disbond from the gelatin as pressure (and thus also the tubing's radius) is changed, leading to air pockets and behavior disparate from real anatomy. Professional ultrasound tissue models are unsuitable for these experiments as they do not have similar elasticity in their vessel analogs; several vendors we investigated used rigid tubing, and all were flow-only (no pressure simulation). Two sizes of tubing were used (2.18 mm radius, "small"; and 3.23 mm radius, "large"). Wall thicknesses of each were 0.25 and 0.28 mm, with a density of 1.93 g/cm measured for both.

The small tubing was submerged to a depth of 2–3 cm in the water/psyllium fiber bath, modeling a depth similar to that of the human carotid artery. Psyllium fiber was used as a scattering medium to simulate surrounding tissue. The tubing was filled with water and inflated using a syringe to add pressure. Pressure was held constant for the course of a scan. Each scan consisted of a stimulus sweep from 200 to 600 Hz in 10 Hz steps with simultaneous measurement using the ultrasound transducer. Five scans were performed at each pressure, and pressure was swept from 60 to 150 mmHg (targeting a physiologically relevant range) in 5 mmHg increments, for a total of 95 scans.

The experiment was repeated using the larger diameter tubing to confirm that the model holds across different vessel sizes. Pressures were swept from 60 to 150 mmHg in 10 mmHg increments. Above 130 mmHg, we found that the tubing would start to rapidly expand in an uneven manner (where the radii of specific segments would expand unevenly, as normally seen during inflation). As this behavior is not seen in healthy arteries, we discarded data above 130 mmHg, for a total of 40 scans.

Measurement apparatus

We constructed a custom ultrasound device to provide full insight into the signal processing chain and to allow accurate timing between the resonance-driving stimulus and ultrasound measurement. This device is comprised of two USRP N210 software-defined radios (National Instruments, Austin, TX, USA), tied to custom transmit and receive electronics. The transmit chain consists of a threshold block, followed by a bipolar high-voltage pulse generator (a MAX4940, from Maxim Electronics, San Jose, CA, USA). The receive chain consists of a matching network and low-noise amplifier with voltage-controlled gain (an AD8336 from Analog Devices, Wilmington, MA, USA). The gain is set via software and provides time-gain compensation. These chains are isolated from one another via an automatic transmit–receive switch (a MD0100 from Microchip, Chandler, AZ, USA). The device has one transmit chain and two receive chains, which are multiplexed to 32 ultrasound transducer pixels. In addition, the device has an amplified low-voltage output which feeds the audio-frequency stimulus transducers.

Downstream of the transmit/receive electronics, a commercial 6L3 linear ultrasound probe (Acuson, Mountain View, CA, USA) provides conversion to ultrasound. Audio-frequency stimulus is provided by a set of audio-frequency bone conduction transducers (BC-10 from Ortofon, Nakskov, Denmark), mounted to the Acuson 6L3.

Capture bandwidth of the software-defined radios and associated electronics extends to 25 MHz, allowing for adequate localization and image reconstruction of pulses ranging from 3 to 6 MHz. Raw data are captured for post-processing by custom software.

Arterial mock-up data analysis

For each individual scan, radius was calculated from the average delay in echo timings between the top and bottom walls, and resonant frequency was calculated using the Vector Fitting method described above. Because the tubing walls were much thinner than those of in vivo arteries, thickness could not be determined accurately from our ultrasound imaging due to limited resolution. Instead, we used high-precision calipers to measure the unpressurized radius and thickness of the tubing (a_0 and h_0). Because the tubing was assumed to be incompressible ($\nu = 0.5$), a pressure-dependent thickness could be calculated as $h = h_0 \times (r_0/r)$. These caliper measurements along with the weight of the tubing were also used to calculate its density.

The Young's modulus of the tubing was calculated by comparing radius and resonant frequency measurements across multiple scans at different pressures, as described above. We assumed that the tubing was linearly elastic, so a single value of E was calculated which minimized the relative error in pressure as determined by Equations 21 and 28; this value came out to roughly 1.16 MPa. The balloon material was later analyzed with a tensile strength measurement instrument from Instron (Norwood, MA, USA). This test yielded an average stiffness of 1.10 MPa which held nearly constant across our strain range, validating both our calculated value and our linearity assumption.

Measured radii were adjusted for each scan based on this fixed E value to generate agreement between these two equations. For the larger tubing, obtaining alignment with theory required adding $h/2$ to all radii; this would be explained if peak echoes from this system corresponded to the inner rather than average radius of the tube. The measured values for radius, thickness, resonant frequency, and stiffness were combined with prior values for wall density, fluid density, and wall Poisson's ratio in Equation 21 to generate the final calculated pressure values shown in Fig. 3.

Human feasibility studies: design and data collection

Study 1

This study was a prospective observational feasibility study evaluating the carotid, brachial, axillary, and femoral arteries in a single test subject compared to a BP cuff. Before each scan with the RSM device, the subject took a single oscillometric BP cuff measurement (SBP and DBP estimates from the cuff are displayed as gray dashed lines in Fig. 5). This study was developed under guidelines for self-experimentation (56), and one of the authors both collected the data and served as the subject over several sessions in 2022 and 2023. The study was undertaken in order to evaluate the feasibility of data collection in multiple arteries of one subject. Data were analyzed to produce arterial pressure waveforms displayed in Fig. 5; no further analysis was conducted.

Study 2

This study was a prospective observational, first-in-human feasibility study evaluating the carotid arteries in six test subjects (Table S3) compared to a BP cuff. The research protocol was approved by the California Institute of Technology (protocol no. 19-0971). Consent was obtained from all participants in the study. The aim of this study was to assess feasibility of collecting data in a single artery across multiple subjects for the sole purpose of demonstrating that resonance phenomena exist in humans. Study 2 evaluated the carotid artery in six volunteer test subjects in comparison with a BP cuff. Recruitment and data collection

occurred during one session in October 2022. Data were collected with the BP cuff on the arm ipsilateral to the device placed on the carotid artery [IEEE Std 1708a-2019 (57) and ISO 81060-2 (58)]. Two measurements were taken with the BP cuff prior to initial data collection. Five 1-minute measurements were taken with the device, and then, two additional BP cuff measurements were taken. An additional five 1-minute device measurements were taken, and finally, two additional BP cuff measurements were taken at the completion of data collection. Data were analyzed for SBP and DBP as well as arterial waveform presence and shape. Statistical analyses were completed using SigmaPlot 15.0 (Systat Software Inc) and MATLAB 2022a (MathWorks). A power analysis was completed assuming alpha of 0.05 and power of 0.80 with an estimated effect size of 5 mmHg. In a study using a *t*-test to compare two methods, a sample of 20 measurements can be used to determine a difference between the two datasets. Statistics were calculated according to universal standard ISO 81060-2.

It should be noted that, as an early feasibility study demonstrating proof-of-concept, strict adherence to regulatory standards was not intended, specifically in relation to subject numbers. This study was designed only to demonstrate that arterial resonance is observable in human arteries. Existing standards such as IEEE 1708 and ISO 81060-2 were not designed for cuffless, continuous, calibration-free devices and thus are not entirely appropriate for demonstration of this technology; however, we attempted to follow the static testing guidelines in IEEE 1708 and 81060-2 as closely as possible. ISO 81060-3 (59) had not yet been published at the time of data collection. It is likely a new set of procedures will need to be developed for future regulatory testing of this device.

Data processing pipeline for BP calculation

To calculate BP, we extracted the necessary physical measurements required by the model (i.e. radius, resonance frequency, and thickness) from the ultrasound imaging. Using a custom data processing pipeline, we were able to extract the relevant measurements from the raw ultrasound data and produce a BP estimate. A detailed outline of the data processing pipeline is shown in Fig. S1, with the key steps briefly summarized below. Using ultrasound imaging at a frame rate of ~300 Hz, we visualized the pulsatile artery walls in each subject and segmented them to extract instantaneous radius and thickness measurements (Fig. S3, Movie S1). Using simultaneously captured Doppler ultrasound data, we also measured arterial wall velocities generated by our stimulus and used this response to identify the arterial resonant frequency at a rate of 200 Hz (Movie S1). User-specified indicators for the locations of the artery walls were also provided to aid in distinguishing the location of arterial walls within the image from other vasculature. The instantaneous elastic modulus was estimated continuously to account for the nonlinear elasticity of the arterial wall (Materials and methods, Supplementary Text S1.2). A Kalman filter was used to combine wall velocity and image-derived radius and thickness measurements, providing a better estimate of both radius and thickness. These data were then fed into our stiffness calculator and the BP formula (Equation 1 in the main text). The resulting BP estimates were low-passed to remove unphysical high-frequency noise and then screened using a set of quality control criteria to remove data contaminated by artifacts stemming from the manual operation of the device, such as excessive motion of either the probe or subject.

Quality control criteria and data exclusion

BP measurements obtained from the test device were processed using standard methods from the literature that are consistent with those employed by vital sign monitors (60). First, measurements were passed through an interquartile range filter and a 12-Hz low-pass filter. To convert continuous measurements into clinically relevant metrics of DBP and SBP, data were divided into nonoverlapping time windows with a length of 6 seconds, rounded to the nearest heartbeat interval. For each window, DBP and SBP were calculated as the average of peak minima and maxima, respectively.

Because a manual placement of the probe is required for the current implementation of the device, measurements are highly sensitive to motion-induced operator error, including shifts due to operator fatigue, as well as test subject movement. As a result, signal loss was a regular occurrence and these data were deemed unusable and excluded from the final analysis.

Reference continuous pressure waveform from BP cuff

A reference for the arterial BP at the carotid artery was calculated in Fig. 6 using the calibrated exponential function proposed by Meinders and Hoeks (34). This empirically derived relationship provides a method to obtain localized BP from arterial radius waveforms by first calibrating the fitting parameters in the equation to a separate BP reference, such as a brachial sphygmomanometer, when measurements from an arterial catheter are unavailable. This method has been employed in numerous previous studies as a means of extrapolating instantaneous BP information from arterial dimensions obtained with ultrasound imaging (17–20, 61). Assuming that the target artery has a circular interior cross section and exhibits minimal hysteresis, the pressure–radius relationship is given by

$$P(r) = P_{\mathrm{dia}} \exp\left[\alpha\left(\frac{r^2}{r_{\mathrm{dia}}^2} - 1\right)\right] \tag{30}$$

where α is an artery-specific stiffness coefficient given by

$$\alpha = \frac{r_{\mathrm{dia}}^2}{r_{\mathrm{sys}}^2 - r_{\mathrm{dia}}^2} \ln\left[\frac{P_{\mathrm{sys}}}{P_{\mathrm{dia}}}\right] \tag{31}$$

Here, P is the arterial pressure, r is the arterial radius, and the $_{\mathrm{dia}}$ and $_{\mathrm{sys}}$ subscripts indicate the diastolic and systolic values of the given parameters, respectively.

While r and r_{dia} can be measured directly with ultrasound at the target location, P_{dia}, P_{sys}, and, subsequently, α are not known a priori from passive ultrasound imaging and must be informed by an external BP reference, in this case, a BP cuff (Philips Intellivue MP70).

Because the reference BP measurement might not be collected with the measurements of the arterial dimensions, as is the case of the present carotid artery measurements, Meinders and Hoeks (34) suggested a correction whereby α is iteratively updated until the mean BP obtained from the exponential fit matches that obtained from the reference. This approach operates under the assumption that the DBP and mean BP do not vary significantly in the various arteries, unlike systolic BP (62). In the present study, α is first estimated using Equation 31 and then updated using

$$\alpha_{i+1} = \left(\left(\frac{\overline{P_{\mathrm{ref}}}}{\frac{1}{T}\int_{t_0}^{t_0+T} P(r(t))dt} - 1\right)\beta + 1\right)\alpha_i \tag{32}$$

where $\overline{P_{ref}}$ is the reference mean BP and β is a dimensionless over-relaxation factor to accelerate convergence. In instances where the mean BP is not available, as can often be the case for brachial sphygmomanometer, $\overline{P_{ref}}$ can be estimated using the formula proposed by Meaney et al. (63):

$$\overline{P_{ref}} = P_{dia} + 0.412(P_{sys} - P_{dia}) \quad (33)$$

Iterative updating of α is conducted until the integrated estimate for mean BP is within ± 0.01 mmHg of $\overline{P_{ref}}$, which typically occurs with $\mathcal{O}(10)$ iterations.

Acknowledgments

The authors would like to acknowledge Dr. Mikhail Shapiro and Bill Ling for early access to a Verasonics instrument for preliminary arterial mock-up imaging. The authors thank Laura Gleason for illustrations in figure panels. The authors would like to thank Lynne Rollins for her contributions and Dr. Soheil Saadat for his discussions regarding statistical analysis.

Supplementary Material

Supplementary material is available at *PNAS Nexus* online.

Funding

The authors are grateful to Charlie Trimble, the Carver Mead Innovation Fund, the Grubstake Grant, Maverick Capital, and the California Institute of Technology for funding and resources which made these studies possible.

Author Contributions

A.R., A.B.R., D.Y., and Y.A.-M. conceived the method and worked through initial feasibility studies. R.J. designed the device, developed key algorithms and software, and performed initial analysis. S.D. helped with arterial mock-up data collection and experimental setup. A.B.R., W.P.D., M.K.F., A.C.R., and D.Y. performed data analysis. W.P.D., M.K.F., A.C.R., and D.Y. also performed algorithm development. A.B.R. and R.J. designed clinical studies. Clinical data were collected and analyzed by W.P.D., M.K.F., A.C.R., D.Y., R.J., and A.B.R. Y.A.-M. helped with data analysis and model development. All authors contributed to the drafting and revision of the manuscript.

Preprints

This manuscript was posted on a preprint: https://doi.org/10.1101/2023.12.24.23300502.

Data Availability

All data are available in the manuscript or the supplementary materials.

References

1 Mark JB. 1998. Direct arterial blood pressure monitoring: normal waveforms. In *Atlas of cardiovascular monitoring*. New York: Churchill Livingstone Inc. p. 91–98.
2 Chemla D, *et al.* 2008. Subendocardial viability ratio estimated by arterial tonometry: a critical evaluation in elderly hypertensive patients with increased aortic stiffness. *Clin Exp Pharmacol Physiol*. 35:909–915.
3 Moody GB, Lehman LH. 2009. Predicting acute hypotensive episodes: the 10th annual PhysioNet/computers in cardiology challenge. In Proceedings of Computers in Cardiology Conference; Park City, Utah, USA. IEEE. p. 541–544.
4 Nuttall G, *et al.* 2016. Surgical and patient risk factors for severe arterial line complications in adults. *Anesthesiology*. 124:590–597.
5 Sharman JE, *et al.* 2022. Automated 'oscillometric' blood pressure measuring devices: how they work and what they measure. *J Hum Hypertens*. 37:93–100.
6 Kallioinen N, Hill A, Horswill MS, Ward HE, Watson MO. 2017. Sources of inaccuracy in the measurement of adult patients' resting blood pressure in clinical settings: a systematic review. *J Hypertens*. 35:421–441.
7 Bur A, *et al.* 2000. Accuracy of oscillometric blood pressure measurement according to the relation between cuff size and upper-arm circumference in critically ill patients. *Crit Care Med*. 28:371–376.
8 Viera AJ, Lingley K, Hinderliter AL. 2011. Tolerability of the Oscar 2 ambulatory blood pressure monitor among research participants: a cross-sectional repeated measures study. *BMC Med Res Methodol*. 11:59.
9 Muntner P, *et al.* 2019. Measurement of blood pressure in humans: a scientific statement from the American Heart Association. *Hypertension*. 73:e35–e66.
10 Imholz BPM, Wieling W, van Montfrans GA, Wesseling KH. 1998. Fifteen years experience with finger arterial pressure monitoring: assessment of the technology. *Cardiovasc Res*. 38:605–616.
11 Salvi P, Grillo A, Parati G. 2015. Noninvasive estimation of central blood pressure and analysis of pulse waves by applanation tonometry. *Hypertens Res*. 38:646–648.
12 Quan X, *et al.* 2021. Advances in non-invasive blood pressure monitoring. *Sensors (Basel)*. 21:4273.
13 Shaltis P, Reisner A, Asada H. 2005. Calibration of the photoplethysmogram to arterial blood pressure: capabilities and limitations for continuous pressure monitoring. In 2005 IEEE Engineering in Medicine and Biology 27th Annual Conference; Shanghai, China. IEEE. p. 3970–3973.
14 Ibrahim B, Jafari R. 2019. Cuffless blood pressure monitoring from an array of wrist bio-impedance sensors using subject-specific regression models: proof of concept. *IEEE Trans Biomed Circuits Syst*. 13:1723–1735.
15 Mukkamala R, *et al.* 2015. Toward ubiquitous blood pressure monitoring via pulse transit time: theory and practice. *IEEE Trans Biomed Eng*. 62:1879–1901.
16 Kim C-S, Carek AM, Inan OT, Mukkamala R, Hahn J-O. 2018. Ballistocardiogram-Based approach to cuff-less blood pressure monitoring: proof-of-concept and potential challenges. *IEEE Trans Biomed Eng*. 65:2384–2391.
17 Beulen BWAMM, *et al.* 2011. Toward noninvasive blood pressure assessment in arteries by using ultrasound. *Ultrasound Med Biol*. 37:788–797.
18 Vappou J, Luo J, Okajima K, Di Tullio M, Konofagou EE. 2011. Non-invasive measurement of local pulse pressure by pulse wave-based ultrasound manometry (PWUM). *Physiol Meas*. 32:1653–1662.
19 Seo J, Lee H-S, Sodini CG. 2021. Non-invasive evaluation of a carotid arterial pressure waveform using motion-tolerant ultrasound measurements during the Valsalva Maneuver. *IEEE J Biomed Health Inform*. 25:163–174.
20 Wang C, *et al.* 2018. Monitoring of the central blood pressure waveform via a conformal ultrasonic device. *Nat Biomed Eng*. 2:687–695.

21 Zakrzewski AM, Huang AY, Zubajlo R, Anthony BW. 2018. Real-Time blood pressure estimation from force-measured ultrasound. *IEEE Trans Biomed Eng*. 65:2405–2416.
22 Avolio A, *et al.* 2022. Challenges presented by cuffless measurement of blood pressure if adopted for diagnosis and treatment of hypertension. *Pulse*. 10:34–45.
23 Kawano Y. 2011. Diurnal blood pressure variation and related behavioral factors. *Hypertens Res*. 34:281–285.
24 Deegan BM, *et al.* 2011. The effect of blood pressure calibrations and transcranial Doppler signal loss on transfer function estimates of cerebral autoregulation. *Med Eng Phys*. 33:553–562.
25 Volovici V, Syn NL, Ercole A, Zhao JJ, Liu N. 2022. Steps to avoid overuse and misuse of machine learning in clinical research. *Nat Med*. 28:1996–1999.
26 Arnold RN, Warburton GB. 1949. Flexural vibrations of the walls of thin cylindrical shells having freely supported ends. *Proc R Soc London Ser A Math Phys Sci*. 197:238–256.
27 Korteweg DJ. 1878. Ueber die Fortpflanzungsgeschwindigkeit des Schalles in elastischen Röhren. *Ann Phys*. 241:525–542.
28 Bramwell JC, Hill AV. 1922. The velocity of pulse wave in man. *Proc R Soc London Ser B Containing Pap Biol Charact*. 93:298–306.
29 Fung YC, Sechler EE, Kaplan A. 1957. On the vibration of thin cylindrical shells under internal pressure. *J Aerosp Sci*. 24:650–660.
30 Lindholm US, Kana DD, Abramson HN. 1962. Breathing vibrations of a circular cylindrical shell with an internal liquid. *J Aerosp Sci*. 29:1052–1059.
31 Warburton GB. 1961. Vibration of a cylindrical shell in an acoustic medium. *J Mech Eng Sci*. 3:69–79.
32 Hasgall PA, *et al.* 2022. IT'IS Database for thermal and electromagnetic parameters of biological tissues, Version 4.1, Feb 22, 2022. https://doi.org/10.13099/VIP21000-04-1.
33 Gustavsen B, Semlyen A. 1999. Rational approximation of frequency domain responses by vector fitting. *IEEE Trans Power Delivery*. 14:1052–1061.
34 Meinders JM, Hoeks APG. 2004. Simultaneous assessment of diameter and pressure waveforms in the carotid artery. *Ultrasound Med Biol*. 30:147–154.
35 Pauca AL, Wallenhaupt SL, Kon ND, Tucker WY. 1992. Does radial artery pressure accurately reflect aortic pressure? *Chest*. 102:1193–1198.
36 Armstrong MK, *et al.* 2019. Brachial and radial systolic blood pressure are not the same. *Hypertension*. 73:1036–1041.
37 Boutouyrie P, *et al.* 1999. Association between local pulse pressure, mean blood pressure, and large-artery remodeling. *Circulation*. 100:1387–1393.
38 Kollias A, Lagou S, Zeniodi ME, Boubouchairopoulou N, Stergiou GS. 2016. Association of central versus brachial blood pressure with target-organ damage: systematic review and meta-analysis. *Hypertension*. 67:183–190.
39 Safar ME, *et al.* 2002. Central pulse pressure and mortality in end-stage renal disease. *Hypertension*. 39:735–738.
40 Trudeau L. 2014. Central blood pressure as an index of antihypertensive control: determinants and potential value. *Can J Cardiol*. 30:S23–S28.
41 Agabiti-Rosei E, *et al.* 2007. Central blood pressure measurements and antihypertensive therapy: a consensus document. *Hypertension*. 50:154–160.
42 Mukkamala R, Xu D. 2010. Continuous and less invasive central hemodynamic monitoring by blood pressure waveform analysis. *Am J Physiol Heart Circ Physiol*. 299:H584–H599.
43 Scheer BV, Perel A, Pfeiffer UJ. 2002. Clinical review: complications and risk factors of peripheral arterial catheters used for haemodynamic monitoring in anaesthesia and intensive care medicine. *Crit Care*. 6:199–204.
44 Picone DS, *et al.* 2017. Accuracy of cuff-measured blood pressure: systematic reviews and meta-analyses. *J Am Coll Cardiol*. 70:572–586.
45 Celler BG, *et al.* 2021. Are Korotkoff sounds reliable markers for accurate estimation of systolic and diastolic pressure using brachial cuff sphygmomanometry? *IEEE Trans Biomed Eng*. 68:3593–3601.
46 Narloch JA, Brandstater ME. 1995. Influence of breathing technique on arterial blood pressure during heavy weight lifting. *Arch Phys Med Rehabil*. 76:457–462.
47 Khamdaeng T, Luo J, Vappou J, Terdtoon P, Konofagou EE. 2012. Arterial stiffness identification of the human carotid artery using the stress-strain relationship in vivo. *Ultrasonics*. 52:402–411.
48 Marque V, van Essen H, Struijker-Boudier HAJ, Atkinson J, Lartaud-Idjouadiene I. 2001. Determination of aortic elastic modulus by pulse wave velocity and wall tracking in a rat model of aortic stiffness. *J Vasc Res*. 38:546–550.
49 Karimi A, Sera T, Kudo S, Navidbakhsh M. 2016. Experimental verification of the healthy and atherosclerotic coronary arteries incompressibility via digital image correlation. *Artery Res*. 16:1–7.
50 Carew TE, Vaishnav RN, Patel DJ. 1968. Compressibility of the arterial wall. *Circ Res*. 23:61–68.
51 Papadacci C, *et al.* 2018. Non-invasive evaluation of aortic stiffness dependence with aortic blood pressure and internal radius by shear wave elastography and ultrafast imaging. *IRBM*. 39:9–17.
52 Hedrick WR, Hykes DL. 1995. Autocorrelation detection in color Doppler imaging: a review. *J Diagn Med Sonogr*. 11:16–22.
53 Earle M, De Portu G, DeVos E. 2016. Agar ultrasound phantoms for low-cost training without refrigeration. *Afr J Emerg Med*. 6:18–23.
54 Richardson C, Bernard S, Dinh VA. 2015. A cost-effective, gelatin-based phantom model for learning ultrasound-guided fine-needle aspiration procedures of the head and neck. *J Ultrasound Med*. 34:1479–1484.
55 Bude RO, Adler RS. 1995. An easily made, low-cost, tissue-like ultrasound phantom material. *J Clin Ultrasound*. 23:271–273.
56 Hanley BP, Bains W, Church G. 2019. Review of scientific self-experimentation: ethics history, regulation, scenarios, and views among ethics committees and prominent scientists. *Rejuvenation Res*. 22:31–42.
57 IEEE Standards Committee. 2019. 1708a-2019: IEEE Standard for wearable, cuffless, blood pressure measuring devices: Amendment 1.
58 ISO Standards Committee. 2018. ISO 81060-2:2018: Non-invasive sphygmomanometers—Part 2: clinical investigation of intermittent automated measurement type.
59 ISO Standards Committee. 2022. ISO 81060-3:2022: Non-invasive sphygmomanometers—Part 3: clinical investigation of intermittent automated measurement type.
60 Pasma W, Peelen LM, van Buuren S, van Klei WA, de Graaff JC. 2020. Artifact processing methods influence on intraoperative hypotension quantification and outcome effect estimates. *Anesthesiology*. 132:723–737.
61 Wang C, *et al.* 2022. Bioadhesive ultrasound for long-term continuous imaging of diverse organs. *Science*. 377:517–523.
62 Nichols WW, O'Rourke M, Vlachopoulos C. 2011. *McDonald's blood flow in arteries: theoretical, experimental and clinical principles*. London, UK: CRC Press.
63 Meaney E, *et al.* 2000. Formula and nomogram for the sphygmomanometric calculation of the mean arterial pressure. *Heart*. 84:64.